Landslide generated impulse waves. 1. Instantaneous flow fields

H.M. Fritz, W.H. Hager, H.-E. Minor

Abstract Landslide generated impulse waves were investigated in a two-dimensional physical laboratory model based on the generalized Froude similarity. Digital particle image velocimetry (PIV) was applied to the landslide impact and wave generation. Areas of interest up to 0.8 m by 0.8 m were investigated. The challenges posed to the measurement system in an extremely unsteady three-phase flow consisting of granular matter, air, and water were considered. The complex flow phenomena in the first stage of impulse wave initiation are: high-speed granular slide impact, slide deformation and penetration into the fluid, flow separation, hydrodynamic impact crater formation, and wave generation. During this first stage the three phases are separated along sharp interfaces changing significantly within time and space. Digital masking techniques are applied to distinguish between phases thereafter allowing phase separated image processing. PIV provided instantaneous velocity vector fields in a large area of interest and gave insight into the kinematics of the wave generation process. Differential estimates such as vorticity, divergence, elongational, and shear strain were extracted from the velocity vector fields. The fundamental assumption of irrotational flow in the Laplace equation was confirmed experimentally for these non-linear waves. Applicability of PIV at large scale as well as to flows with large velocity gradients is highlighted.

H.M. Fritz (✉), W.H. Hager, H.-E. Minor
Laboratory of Hydraulics,
Hydrology and Glaciology (VAW),
Swiss Federal Institute of Technology (ETH),
CH-8092 Zurich, Switzerland
E-mail: hermann.fritz@gtrep.gatech.edu
Tel.: +1-912-9667947
Fax: +1-912-9667836

Present address: H.M. Fritz
Georgia Institute of Technology,
210 Technology Circle,
Savannah, GA 31407, USA

List of symbols

a	wave amplitude (L)
c	wave celerity (LT^{-1})
d_{diff}	diffraction limited minimum particle image diameter (L)
d_{e}	diffracted particle image diameter (L)
d_{g}	granulate grain diameter (L)
d_{p}	seeding particle diameter (L)
d_{τ}	recorded particle image diameter (L)
f	focal length (L)
$f_{\#}$	f number (-)
$\mathbf{F}$	slide Froude number (-)
g	gravitational acceleration (LT^{-2})
h	still-water depth (L)
H	wave height (L)
l_{s}	slide length (L)
L	wavelength (L)
M	magnification (-)
m_{s}	slide mass (M)
n	refractive index (-)
n_{por}	slide porosity (-)
N_{iw}	number of seeding particles in an interrogation window (-)
N_{pair}	number of detected particle image pairs in window (-)
p	interrogation window size $p{\times}p$ pixels; 1 pixel=9 μm (L)
P	probability (-)
P_{il}	probability of in-plane loss of particle (-)
P_{ol}	probability of out-of-plane loss of particle (-)
s	slide thickness (L)
S	relative slide thickness (-)
t	time after impact (T)
T	wave period (T)
v	velocity (LT^{-1})
v_{p}	particle velocity (LT^{-1})
v_{px}	streamwise horizontal component of particle velocity (LT^{-1})
v_{py}	crosswise horizontal component of particle velocity (LT^{-1})
v_{pz}	vertical component of particle velocity (LT^{-1})
v_{s}	slide centroid velocity at impact (LT^{-1})
V	dimensionless slide volume (-)
V_{iw}	interrogation volume (L^3)
V_{s}	slide volume (L^3)
x	streamwise coordinate (L)
x_{ip}	area of view x dimension in image plane (L)
z	vertical coordinate (L)
α	slide impact angle (°)

δ	bed friction angle (°)
δy	depth of field (L)
Δt	laser pulse separation (T)
Δx	mean particle image x displacement in interrogation window (L)
$\varepsilon_{\Delta x}$	random displacement Δx error (L)
ε_v	random velocity v error (LT^{-1})
ε_{tot}	total random velocity v error (LT^{-1})
ε_{bias}	velocity v error due to biased correlation analysis (LT^{-1})
ε_{optics}	velocity v error due to optical imaging errors (LT^{-1})
ε_{track}	velocity v error due to particle flow tracking error (LT^{-1})
ε_{xx}	streamwise horizontal elongational strain component (1/T)
ε_{xz}	shear strain component (1/T)
ε_{zx}	shear strain component (1/T)
ε_{zz}	vertical elongational strain component (1/T)
η	water surface displacement (L)
λ	wavelength (L)
μ	dynamic viscosity (ML^{-1}T^{-1})
ρ	density (ML^{-3})
ρ_g	granulate density (ML^{-3})
ρ_p	particle density (ML^{-3})
ρ_s	mean slide density (ML^{-3})
ρ_w	water density (ML^{-3})
φ'	granulate internal friction angle (°)
ω_y	vorticity vector component (out-of-plane) (1/T)

1
Introduction

Large water waves may be generated by landslides, shore instabilities, snow avalanches, glacier, and rock falls in geometrically confined water bodies such as reservoirs, lakes, and bays (Slingerland and Voight 1979). For Alpine lakes, impulse waves are particularly significant, because of steep shores, narrow reservoir geometries, possible large slide masses, and high impact velocities. The resulting impulse waves can cause disaster owing to run-up along the shoreline and overtopping of dams (Vischer and Hager 1998). The wave generating mass flows may be subdivided into high-density rock and soil movements, and low-density glacier falls and snow avalanches. Herein only impulse waves generated by landslides are considered. Landslides contributed to the most destructive impulse waves in recorded history. The term landslide is widely used for almost all varieties of slope movements (Varnes 1978). The classification of the landslide and water body interaction is based on the initial position of the landslide relative to the still-water surface. Three categories are commonly used: subaerial landslide impacts, partially submerged landslides, and subaqueous or submarine landslides. Only subaerial landslide impacts into water bodies are considered herein. For subaerial landslide impacts, three phases are relevant: slide material, water, and air. The impulse wave phenomenon may be subdivided into three main phases. The first stage involves the whole wave generation process with the landslide impact and the run-out along the bed of the water body, the water displacement, and the wave formation. The second stage embraces the propagation of the impulse wave train over the water body including lateral spreading and dispersion. The third stage is characterized by the wave run-up along the shoreline and includes also the transformation of the waves with decreasing water depth. The focus of the present study is on the wave generation process and the near field wave propagation in a two-dimensional physical model. The radial wave propagation in a three-dimensional physical model was investigated by Huber (1980). The wave run-up is referred to in Müller (1995). Subaerial rockslide impacts into water bodies with the subsequent wave generation and propagation were considered in a two-dimensional Froude similarity model. The recorded wave profiles were extremely unsteady and non-linear. Four wave types were determined: weakly non-linear oscillatory waves, non-linear transition waves, solitary-like waves, and dissipative transient bore (Fritz 2002b). Most of the generated impulse waves were located in the intermediate water depth wave regime. The physical model results were compared to the giant rockslide generated impulse wave, which struck the shores of the Lituya Bay, Alaska, in 1958. The measurements obtained in the physical model were in agreement with the in-situ data (Fritz et al. 2001). Herein only three characteristic instantaneous velocity-vector field sequences obtained by particle image velocimetry (PIV) are presented. Further data sets are included in Fritz (2002b). The kinematics of the wave generation process are discussed.

2
Physical model

The granular rockslide impact experiments were conducted in a rectangular prismatic water wave channel, 11 m long, 0.5 m wide, and 1 m deep with varying still-water depths h=0.30, 0.45, and 0.675 m. A 3-m long hill slope ramp was built into the front end of the channel. The hill slope angle α was variable from 30° to 90°. In the present study only the angle α=45° was considered.

The landslides were modeled with an artificial granular material (PP-BaSO$_4$) having the exact grain density ρ_g=2.64 t/m^3 of common natural rock formations such as granite, limestone, sandstone, and basalt. Natural rock densities vary roughly within 2–3.1 t/m^3 concentrating around 2.6–2.7 t/m^3 (De Quervain 1980; Kündig et al. 1997). The granular material consisted of 87% (weight percentage) barium-sulphate (ρ=4.5 t/m^3) compounded with 13% polypropylene (ρ=0.91 t/m^3). The slide granulate consisted of cylindrical grains with a mono-disperse grain diameter d_g=4 mm (Fig. 5a, below). As a bulk granular medium the density is reduced to the slide density ρ_s=1.62 t/m^3 because of the porosity n_{por}=0.39 according to ρ_s=(1−n_{por})ρ_g. The estimated values for the slide density and porosity correspond to the granulate packing in the slide box. The various initial slide shapes filled into the slide box are described by Fritz and Moser (2003). The assumed porosity corresponds to data from granular Alpine debris flows (Tognacca 1999) and the disturbed debris deposits at Mount St. Helens (Glicken 1996). The considered slide masses m_s=27, 54, and 108 kg

were determined to an accuracy of ±0.05 kg. The effective internal friction angle of the granulate was determined to $\varphi'=43°$ in triaxial shear tests. The dynamic bed friction angle was estimated to $\delta=24°$. Hence the slip between the bed and the granular mass was dominant resulting in slug-type flow (Savage 1979). Herein only the regime with $\rho_s > \rho_w$ is considered with one granular material. Other densities with $\rho_s < \rho_w$ relating to glacier breakdowns and snow avalanches remain to be investigated.

The dynamic slide impact characteristics were controlled by means of a novel pneumatic landslide generator, which allowed exact reproduction and independent variation of single dynamic slide parameters within a broad spectrum (Fritz and Moser 2003). The pneumatic landslide generator enabled starting the experiments with controlled initial conditions just before impact, thus allowing exact reproduction and independent variation of single dynamic slide parameters. In particular, different slide impact shapes were produced for the same slide impact velocity and mass. The following four relevant parameters governing the wave generation were varied: granular slide mass m_s, slide impact velocity v_s, still-water depth h, and slide thickness s. The parameters describing impulse waves are shown in Fig. 1.

The main slide parameters are the slide thickness s, the slide length l_s, the slide centroid velocity v_s at impact, and the slide density ρ_s. The water body topography is characterized by the still-water depth h and the hill slope angle α. The origin of the coordinate system (x, z) is at the intersection of the still-water surface with the hill slope. The wave characteristics are described by the wavelength L and the wave height H or the amplitude a. All other parameters, such as wave propagation velocity c and wave period T can be determined theoretically from these quantities. Impulse waves in the near field typically yield different crest and trough amplitudes. The wave gauge recordings at location x as a function of the time t after impact are commonly denoted by η. The main wave characteristics were related to the following three dimensionless quantities: the slide Froude number $\mathbf{F} = v_s/\sqrt{gh}$, the dimensionless slide volume $V = V_s/(bh^2)$ and the dimensionless slide thickness $S=s/h$. The slide Froude number was identified as the dominant parameter relating the slide impact velocity v_s to the shallow water wave propagation velocity $\mathbf{F} = v_s/\sqrt{gh}$. The Froude number $\mathbf{F}$ range covered by the experiments spans roughly from 1 to 4.8. For comparison the Lituya Bay 1958 event had a Froude number $\mathbf{F}=3.2$ determined with a water depth
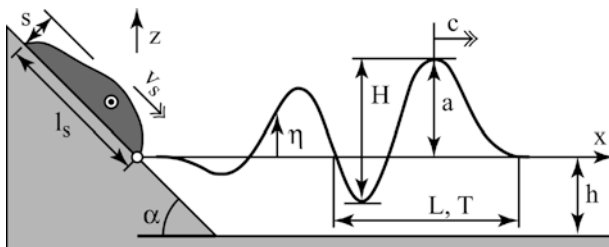
$h=122$ m and a slide impact velocity $v_s=110$ m/s (Fritz et al. 2001). The investigated relative slide thickness S and slide volume V ranged from 0.07 to 0.6 and from 0.07 to 1.6, respectively. It is remarked that other dimensionless numbers may be of importance for other specific results of interest. For example the flow through the granular slide, which depends on the Reynolds number or the Bagnold number, may be used to compare granular flow regimes.

3
Large-scale digital PIV setup

3.1
Instrumentation overview

Three different measurement techniques were built into the physical model: laser distance sensors (LDS), PIV, and capacitance wave gages (CWG). An overview on the implementation and combination of the various systems is shown in Fig. 2. The pneumatics control unit served as trigger master. It controlled the pneumatic landslide generator and synchronized the start of landslide acceleration with the data acquisition of the two measurement PCs, which served as sub-masters. The LDS PC acquired the data from LDSs, CWGs, and the slide box position sensor. The programmable timing unit (PTU) in the PIV PC was the key element for the timing of the whole PIV system. The PTU board received the external TTL (transistor-transistor logic) start trigger from the pneumatics control unit, controlled the CCD-camera exposure and synchronization with the laser pulses. The frame grabber ITI IC-P-4M with acquisition module AM-DIG-16D-XHF (Imaging Technology Inc., Bedford, Mass., USA) in the PIV PC acquired the images from the CCD camera at a data rate of roughly 30 MB/s. The raw images were captured in the RAM of the PIV PC in real time and stored on the hard disks after the experiment.

The granular slide profiles were scanned in the channel axis prior to impact with two LDSs. The optical principle was based on triangulation. The wave features in the propagation area were determined with CWGs. Seven CWGs were positioned along the channel axis with a 1 m spacing. The position of the first wave gage was located at $x=h+1.13$ m given by the landslide run-out (Fritz 2002b).

3.2
Laser light sheet

A twin cavity Nd-YAG laser was used as the light source emitting frequency doubled pulses at 532 nm with a repetition rate of 2×15 Hz and pulse energies of 2×225 mJ at 532 nm (Surelite-PIV, Continuum Inc., Santa Clara, Calif., USA). The operation principle of frequency-doubled Nd-YAG lasers is described by Hecht (1992). In most applications of PIV to water waves, the laser light sheet simply penetrated either vertically through the channel bottom without any disturbing optical components inside the channel (Gray and Greated 1988; Gray et al. 1991; Liu et al. 1992; Skyner 1996; Jensen et al. 2001; among others) or through the water surface (Lin et al., 1999). In this application the splash formed during
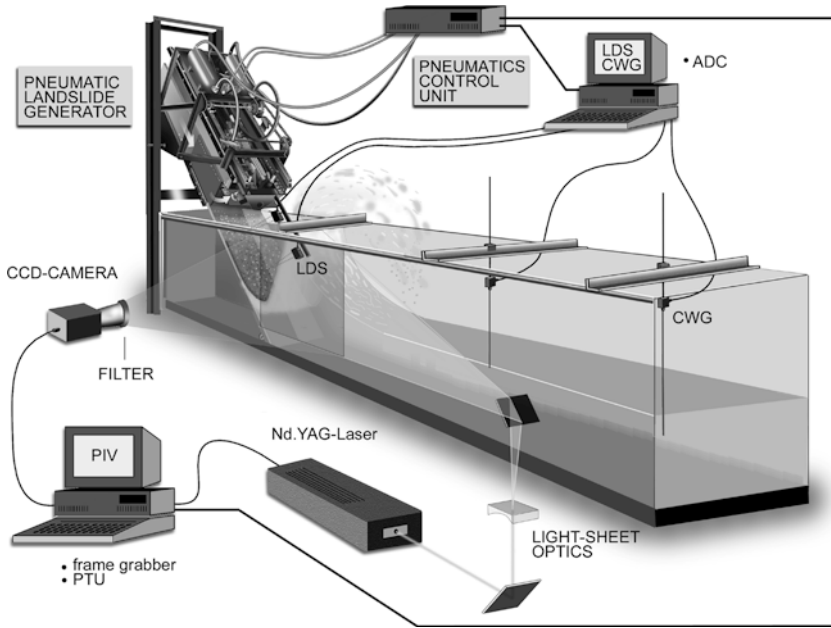
Fig. 1. Definitions of the main slide, water body and impulse wave parameters

Fig. 2. Measurement setup with pneumatic installation and the three measurement systems: LDSs, CWGs and PIV. PIV system with CCD camera twin Nd-YAG laser, simplified light-sheet and beam guiding optics

impact and the slide penetration along the channel bottom denied optical access vertically through the water surface and the channel bottom in the impact area, respectively. Hence the light sheet had to be deflected from downstream into the wave generation area. The light sheet was generated right below the partially glassed bottom of the wave channel using a three-lens configuration (Hecht 1998). The laser light sheet optics and the adjustment principle are shown in Fig. 3b. First, the laser beam was sent through a plano-concave cylindrical lens (focal length $f=-90$ mm), followed by a bi-convex spherical lens ($f=+105$ mm), and finally a plano-concave cylindrical lens ($f=-10$ mm). Altering the distance between the first two lenses allowed light-sheet thickness adjustments whereas changing the distance between the latter lenses adjusted the divergence of the light sheet. The laser beam axis penetrated the glassed channel

bottom under an angle of roughly 80° to avoid aligned back reflections. An underwater mirror deflected the light sheet from up to 4 m downstream axially into the wave generation zone creating a large vertical light sheet. The underwater mirror with a 50 mm diameter is shown in Fig. 3c. The large vertical light sheet is shown in Fig. 3a during a high-speed slide impact experiment. The light sheet in pure tap water had a thickness of 3 mm in the area of interest and roughly tripled to 9 mm with added seeding particles caused by multiple scattering. Only the area of interest was seeded and the focus in the light-sheet thickness was set behind the area of interest to ensure a homogenous scattering intensity distribution within the whole measurement area. The light absorption loss under water may be estimated to 16% using an absorption coefficient of 0.042 m^{-1} for radiation at 532 nm according to Shifrin (1988).
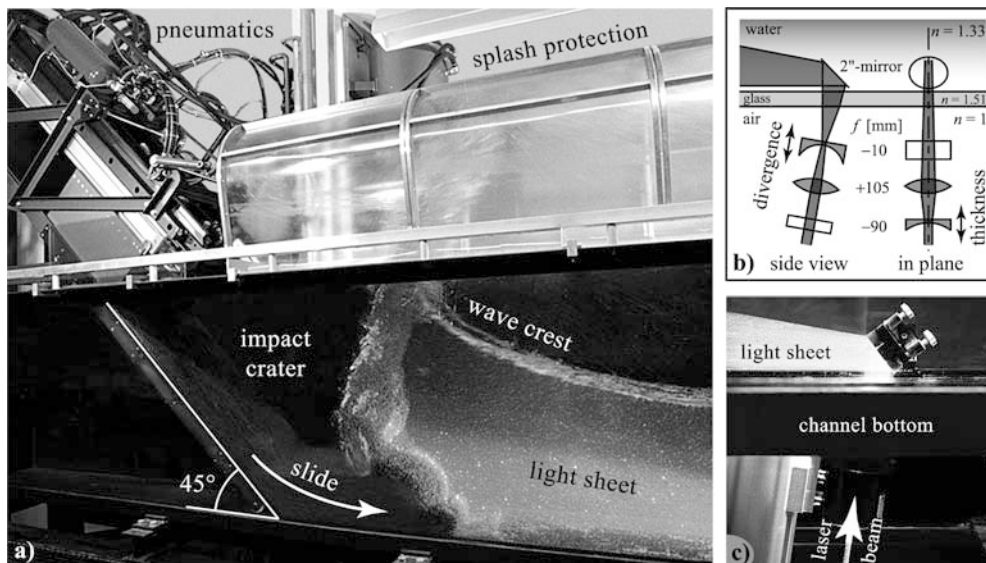

Fig. 3 a Laser light sheet with a $f=-20$ mm plano-concave cylindrical lens (third lens) during a slide impact experiment at **F**=3.3, m_s=108 kg, h=0.45 m and α=45°; **b** light sheet optics and adjustment principle; **c** underwater mirror on channel bottom

3.3
Digital image acquisition

PIV recording was conducted with a mega-resolution progressive scan CCD camera (Holst 1998). The full-frame interline transfer CCD camera (Kodak Megaplus ES1.0DC—Eastman Kodak Co., San Diego, Calif., USA) captured image areas as large as 784(H) mm×765(V) mm reading out 1,008(H)×984(V) pixels. Images were acquired into the RAM of the PC during a maximum of 5 s at a data rate of roughly 30 MB/s—given by the 30 Hz frame rate and the 8-bit pixel depth. The data acquisition was controlled from the analysis software (LaVision GmbH (Goettingen, Germany) DaVis PIV package). Frame straddling was used to expose images in the back-to-back mode (Raffel et al. 1998). The first laser pulse was placed just before the interline transfer, while the second pulse was placed thereafter. The pulse separation Δt was altered within 1 and 17 ms depending on slide impact velocity and area of view. Each pair of back-to-back single exposure images allowed velocity field calculation by means of cross-correlation. With the camera frame rate of 30 Hz the time resolution of the PIV system was a two-dimensional two-component (2D-2C) velocity-vector field estimation at 15 Hz.

A precision measurement objective (Jos. SchneiderOptische Werke GmbH, Bad Kreuznach, Germany: Xenon) with a focal length f=25.6 mm and an f number $f_\#$=1.4 (max. $f_\#$=0.95) was used. The objective had an excellent light transmission of 89% at λ=532 nm, a relative illumination of 84% in the corner of the images at $f_\#$=1.4 and a geometric barrel distortion <0.7 %. A 532 nm linepass filter (FWHM=10 nm; Andover Corp., Salem, N.H., USA) avoided interference with the LDSs at 675 nm and reduced the noise on the second image when working with room light. The reduction of light intensity due to the filter was 30%.

The camera was calibrated with a 1.4 m×0.7 m calibration plate with engraved crosses on a 40 mm grid positioned in the light-sheet plane. Parts of overlaid calibration images acquired with an empty and water-filled wave tank are shown in Fig. 4b. The corresponding geometric imaging is shown in Fig. 4a. The observation distance was roughly 2.3 m with 2.03 m in air (n=1) and 0.25 m under water (n=1.33) separated by 25 mm float glass (n=1.51). The difference in refractive index between air (n=1) and water (n=1.33) bent the ray paths at channel penetration towards the objective axis reducing the underwater image area. The underwater recordings corresponded to images acquired with the virtual camera and an objective with a focal length $f \approx 35$ mm. The magnification factor was M=0.0115 according to Adrian (1991). The depth of field δy was determined to

$$\delta y = 4\left(1 + M^{-1}\right)^2 f_\#^2 \lambda \approx 33 \text{ mm} \tag{1}$$

with λ=532 nm and $f_\#$ = 1.4. The camera position was adjusted to an accuracy of ±1 mm. The geometric barrel distortion was corrected to an accuracy of ±0.1 % with the image correction tool implemented in the analysis software (LaVision GmbH, Goettingen, Germany, DaVis PIV package).

3.4
Seeding particles

Seeding particles with a mono-disperse diameter of d_p=1.6 mm, a density of ρ_p=1.006 g/cm^3 and a refractive index of n=1.52 were used. The Grilamid (L16/20, Ems-Chemie AG, Domat/Ems, Switzerland) seeding particles are shown in Fig. 5b. Particles of this size had to be transparent (absorption coefficient: 0.2 mm^{-1}) and spherical to give round particle images. Opaque particles produced shadow stripes in the light sheet, whereas the images of ground particles were dependent on particle orientation (Bohren and Huffman 1998). The error in PIV velocity measurements strongly depends on the particle image diameter. The optimum particle diameter was determined according to Adrian (1995, 1997). The most important consideration in this large-scale PIV application was to avoid under-sampled particle images according to Nyquist's criterion. Under-sampling leads to both mean bias errors in locating the particle and random errors (Prasad et al. 1992; Wernet and Pline 1993; Westerweel 1993). The uncertainty in velocity detection increases roughly by a factor of 10 for particle images that are too small (Raffel et al. 1998). The recorded particle image diameter d_τ is given approximately by

$$d_\tau = \sqrt{d_e^2 + d_r^2} = 20.6 \ \mu m \tag{2}$$

where d_e is the optical particle image diameter prior to being recorded and d_r=9 μm, given by the pixel spacing, represents the resolution of the CCD sensor. The recorded particle image diameter d_τ corresponded to 2.3 pixels with the CCD pixel diameter of 9 μm (CCD size 9 mm^2). The calculation is confirmed experimentally by the particle images shown in Fig. 5d. This ensured minimum peak detection uncertainty of 0.03 pixels according to Raffel et al. (1998). The diffracted particle image diameter d_e was estimated to

$$d_e = \sqrt{d_{diff}^2 + M^2 d_p^2} = 18.5 \ \mu m \tag{3}$$

with the magnification factor M=0.0115 and the seeding particle diameter d_p=1.6 mm (Goodman 1996). Diffraction
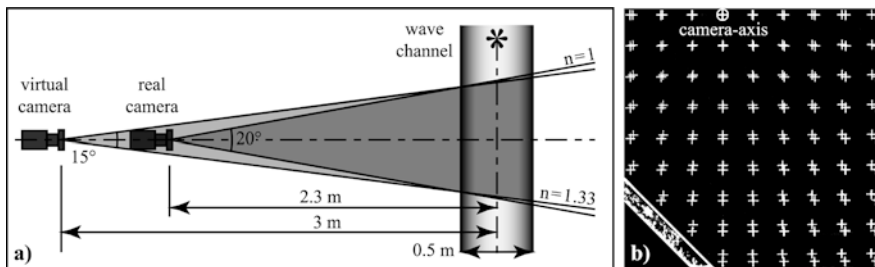
Fig. 4 a Geometric imaging with camera angle of view and refraction in a top view of the experimental setup; **b** overlaid calibration image parts of an in-situ double calibration in air and under water
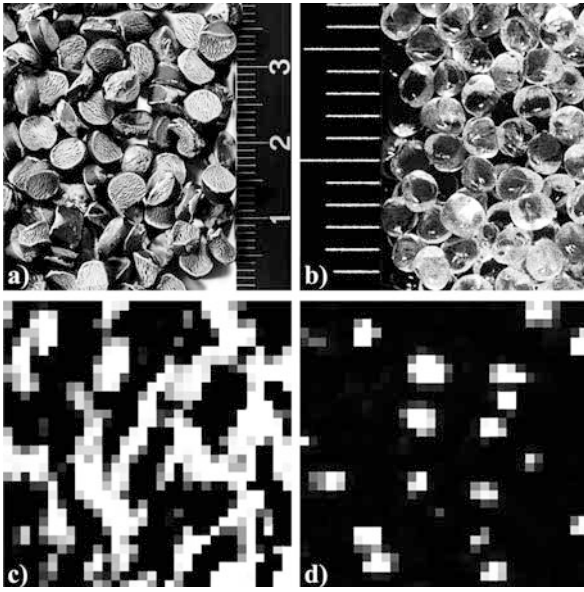
Fig. 5 a Landslide material: PP-BaSO$_4$ granulate with grain diameter d_g= 4 mm, grain density ρ_g=2.64 t/m^3, porosity n_{por}=39% and slide density ρ_s=1.62 t/m^3; **b** seeding particles: Grilamid, d_p=1.6 mm, ρ_p=1.006 g/cm^3; **c** speckle pattern on slide surface in a 32×32 pixels interrogation window; **d** particle image pattern in water

limited imaging and a Gaussian intensity distribution of the geometric particle image were assumed (Adrian and Yao 1985). The diffraction limited minimum image diameter d_{diff} was determined to

$$d_{diff} = 2.44(1 + M)f_\#\lambda \approx 2 \ \mu m \qquad (4)$$

with the laser wavelength λ=532 nm and the diaphragm aperture $f_\#$=1.4. The diffraction limited minimum image diameter d_{diff} was only about 10% of the recorded particle image diameter d_τ. Diffraction contributed less than 1% to the recorded particle image diameter d_τ. Hence the tracer particles with $d_p/\lambda = 3008$ were outside the Mie scattering range and in the geometric optics light scattering range (Mie 1908; Kerker 1969). In the geometric optics light scattering range with $d_p \gg \lambda$ the average energy of the scattered light increases with $(d_p/\lambda)^2$ and the particle image intensity is independent of the particle diameter, as both the scattered light and the image area increase with d_p^2 (van de Hulst 1957). Hence the average particle image intensity was independent of the particle image diameter.

The accuracy of the velocity determination is ultimately limited by the ability of the tracer particles to follow the instantaneous motion of the continuous medium. Most treatments of the behavior of seeding particles use the argument of Stokes for low Reynolds number flow around a sphere. Assuming spherical particles and neglecting the interaction between individual particles, the terminal settling velocity v_p can be derived from Stokes' drag law

$$v_p = \frac{\left(\rho_p - \rho_w\right)d_p^2}{18\mu}g = 8 \ mm/s \qquad (5)$$

with d_p=1.6 mm and ρ_p=1.006 g/cm^3. The vertical drift was two to three orders of magnitude smaller than the

observed peak flow velocities. In a settling experiment some particles drifted to the water surface while others settled down because of a certain variation in particle density, while other particles remained neutrally buoyant over hours. The simple Stokes drag model is not always a sufficient criterion (Melling 1997). There is no need to consider the behavior of particle swarms for the present application. The Basset equation was applied to analyze the flow fidelity of seeding particles beneath water waves (Hering et al. 1997). The Basset equation for particles in an unsteady flow is given by Hinze (1975). The Basset term in the equation accounts for effects of the deviation in flow pattern from steady state. Hjelmfelt and Mockros (1966) presented a solution to the Basset equation for the motion of particles in an oscillatory turbulent flow. In determining the response of seeding particles to an unsteady fluid velocity field, the high frequency part of the spectrum is of interest. If a particle can follow a high-frequency fluctuation, it will track better the low-frequency fluctuations of the large-scale turbulent motion. The usual range of frequencies in turbulent flows reaches up to 10 kHz (Hinze 1975). The computation with the used seeding particles resulted in an error of only 0.4%. This minor slip between particle and ambient fluid is negligible particularly since the slip further reduces at lower frequencies.

3.5
Image analysis

The extremely unsteady three-phase flow consisting of granular matter, water, and air complicated the image analysis and vector-field calculation. The required homogenous flow fields were limited to varying parts of the images. The applied image pre-processing steps are shown in Fig. 6. First the illumination intensity fluctuations in the background were removed with a sliding background subtraction (Jähne 1997). Thereafter the flow field was isolated from the rest of the image with digital masks (Roth et al. 1999; Lindken and Merzkirch 2000). The ramp and the water surface were masked to avoid biased correlation signals caused by total reflections and light scattering of floating seeding particles. The three phases—granular material, water, and air—were separated along distinct interfaces during the decisive initial phase with slide impact, flow separation, crater formation, energy conversion, and wave generation. The use of masking allowed us to distinguish between phases enabling phase separated image processing. Regarding the combined analysis method for PIV in water flow and laser speckle velocimetry (LSV)
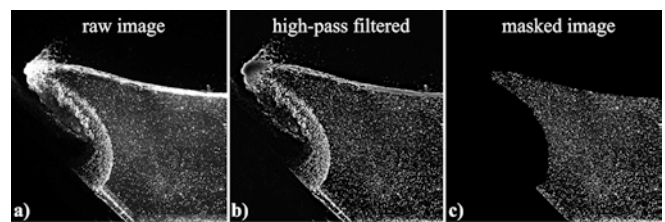
Fig. 6a–c. Pre-processing on the example of a PIV image with first laser pulse illumination—corresponding second frame is not shown. **a** Raw PIV image; **b** high-pass filtered image; **c** masked image

on the corona of the landslide surface it is referred to Fritz (2002a). The mask shown in Fig. 6c isolates the water flow from the rest of the image to evaluate the velocity vector field in the water flow with PIV.

The cross-correlation analysis was conducted using a commercial analysis software (LaVision GmbH, Goettingen, Germany, DaVis PIV package). The instantaneous 2D-2C velocity vector fields were computed with a cross-correlation based adaptive multi-pass algorithm (Scarano and Riethmuller 2000). The advanced digital interrogation method successfully combines several techniques: digital PIV (Willert and Gharib 1991), cross-correlation analysis (Keane and Adrian 1992), discrete window offset (Westerweel et al. 1997), fractional window offset (Scarano and Riethmuller 2000), iterative multi-grid processing with window refinement (Hart 1998; Scarano and Riethmuller 1999), and window distortion (Huang et al. 1993a, 1993b; Fincham and Delerce 2000). The adaptive multi-pass algorithm first calculated a reference vector field from the double image input. A standard cross-correlation interrogation was performed with a relatively large interrogation window size (64×64 pixels) and a mean initial window shift. The calculated vector field determined the window shift for the next higher resolution level with a refined interrogation window size. The iteration was repeated until the final window size (32×32 or 16×16 pixels) was reached.

The second pass at the final window size was conducted with fractional window offsets and window deformations. The software calculated an imaginary vector for each corner of an interrogation window, which determined a deformation tensor for each interrogation window. The window deformation accounted for continuum deformation in terms of rotation, shearing, and dilatation resulting in a better particle matching in regions with large velocity gradients near the slide surface. The amount of spurious vectors in the water flow field was relatively low with roughly 1%. Spurious vectors were determined with a local median filter and a peak ratio or so-called Q-factor (Westerweel 1994; Nogueira et al. 1997).

In practice velocity vectors could be calculated from maximum window displacements up to 20 pixels. Large velocity vectors near the slide front could still be computed from particle image displacements which are larger than the final window sizes using the adaptive multi-pass algorithm since the window shifts were locally adapted to the mean local flow.

3.6
Measurement accuracy
In depth investigations of the different errors involved in PIV with a combination of numerical simulations with synthetic images and experimental benchmark cases were conducted by Huang et al. (1997), Raffel et al. (1998) and Westerweel (2000). The absolute measurement error of a single displacement vector ε_{tot} may be expressed as

$$\varepsilon_{tot} = \varepsilon_{bias} + \varepsilon_v + \varepsilon_{optics} + \varepsilon_{track} \leq 0.07 \text{ m/s} \qquad (6)$$

with a bias error ε_{bias}, a random error ε_v, an optical imaging error ε_{optics} and a particle flow tracking error

ε_{track}. The first two errors arise from the interrogation technique and the latter two from the recording process. By use of the adaptive multi-pass algorithm with window deformation we can cancel the bias error $\varepsilon_{bias} \approx 0$ (Scarano and Riethmuller 2000). The optical imaging error was determined to $\varepsilon_{optics} \leq 0.008$ m/s at a slide impact velocity v_s=8 m/s from uncorrected optical distortions of ±0.1%. The particle flow tracking error was computed to ε_{track}=0.008 m/s with Eq. (5). The random error was computed to $\varepsilon_v \leq 0.05$ m/s from the random displacement error. A conservative assumption was made for the random displacement error $\varepsilon_{\Delta x}$=0.1 pixels defining the minimum resolvable displacement fluctuation (Raffel et al. 1998; Scarano and Riethmuller 2000). The random displacement error $\varepsilon_{\Delta x}$=0.1 pixels corresponds to $\varepsilon_v \leq 0.05$ m/s at a slide impact velocity v_s=8 m/s. The random velocity error ε_v varied proportionally with the maximum particle velocity v_p, because the laser pulse separation Δt was adapted to the maximum flow field velocity of an experiment. Hence the random velocity error decayed to $\varepsilon_v \leq 0.015$ m/s at a slide impact velocity v_s=2.5 m/s. For comparison Son and Kihm (2001) reported a random displacement error of $\varepsilon_{\Delta x}$=0.04 pixels in a similar application of PIV to surface wave breaking and with the same analysis software (LaVision GmbH, Goettingen, Germany, DaVis PIV package).

3.7
Dynamic range and spatial resolution
The performance of the PIV system is described by the dynamic velocity range (DVR), the dynamic spatial resolution (DSR) and the accuracy according to Adrian (1997). The DVR in the x axis was defined as

$$\text{DVR} = \frac{v_{x_{\max}}}{\varepsilon_{v_x}} = \frac{\Delta x_{\max}}{\varepsilon_{\Delta x}} = 160 \qquad (7)$$

with the maximum displacement in the image plane Δx_{max} and the random displacement error $\varepsilon_{\Delta x}$. An analogous definition holds for the z axis. The maximum displacement Δx_{max}=16 pixels in the image plane corresponded to a quarter of the initial interrogation window size of 64×64 pixels, which should not be exceeded after initial window shift subtraction (Keane and Adrian 1990). A conservative assumption was made for the random displacement error $\varepsilon_{\Delta x}$=0.1 pixels defining the minimum resolvable displacement fluctuation. The dynamic spatial range (DSR) was defined as the area of view divided by the smallest resolvable spatial variation. Essentially, this ratio is the same as the number of independent (i.e., non-overlapping) vector measurements that can be made across the linear dimension of the area of view. The dynamic spatial range (DSR) was defined as

$$\text{DSR} = \frac{x_{ip}}{p} = 63 \qquad (8)$$

for an interrogation window size with p=16 pixels and the image plane dimension x_{ip}=1,008 pixels. The dynamic spatial resolution reduced to DSR=31 for an interrogation window size with p=32 pixels. The interrogation window sizes p=16 and 32 pixels correspond to 12.4 and 24.8 mm,

respectively, in the object plane with $M=0.0115$. The particle image density limits the obtainable spatial resolution corresponding to the minimal interrogation window size and has a direct influence on the measurement uncertainty (Raffel et al. 1998). The number of detectable particle image pairs N_{pair} is defined as

$$N_{\mathrm{pair}} = N_{\mathrm{iw}}(1 - P_{il})(1 - P_{ol}) \qquad (9)$$

with the probabilities of in-plane loss of particles P_{il} and out-of-plane loss of particles P_{ol}, respectively (Keane and Adrian 1992). The sample 32×32 pixels interrogation window shown in Fig. 5d contains $N_{\mathrm{iw}}=18$ particles. The in-plane loss of particles approaches $P_{il} \rightarrow 0$ for the applied iterative multi-grid interrogation technique (Scarano and Riethmuller 2000). The macro-scale flow field is well confined to 2D by the physical model and micro-scale turbulent structures are filtered out by the use of large tracer particles. The out-of-plane velocity and accompanying effects such as out-of-plane loss of particles P_{ol} within the laser pulse separation Δt were negligible given the computed divergence fields with roughly zero values. The criteria for valid detection in a final iteration pass is $N_{pair}\geq3$ (Raffel et al. 1998). Hence the minimal final interrogation window size is limited to 16×16 pixels.

3.8
Differential quantities
The applied standard planar PIV provided only the v_{px} and v_{pz} components of the particle velocity vector v_p and the single plain data could only be differentiated in the x and z directions (Raffel et al. 1998). Hence only the following terms of the deformation tensor δv_p were computed

$$\varepsilon_{xx} + \varepsilon_{zz} = \frac{\partial v_{px}}{\partial x} + \frac{\partial v_{pz}}{\partial z} \qquad (10)$$

$$\omega_y = \frac{\partial v_{px}}{\partial z} - \frac{\partial v_{pz}}{\partial x} \qquad (11)$$

$$\varepsilon_{xx} - \varepsilon_{zz} = \frac{\partial v_{px}}{\partial x} - \frac{\partial v_{pz}}{\partial z} \qquad (12)$$

$$\varepsilon_{xz} = \frac{\partial v_{pz}}{\partial x} + \frac{\partial v_{px}}{\partial z} \qquad (13)$$

corresponding to the in-plane divergence $\varepsilon_{xx}+\varepsilon_{zz}$, the out-of-plane vorticity component ω_y, the elongational strain rate $\varepsilon_{xx}-\varepsilon_{zz}$ and the shear strain rate ε_{xz}. Local velocity vector fields resulting in positive estimates of the vorticity, the shear strain and the elongational strain as well as the deformations of the fluid element are shown in Fig. 7a and b, respectively.

A positive vorticity component ω_y corresponds to a driving rotation regarding the breaking of a wave propagating in positive x direction. A positive elongational strain $\varepsilon_{xx}-\varepsilon_{zz}$ corresponds to an elongation of the fluid element along the x axis. The sum of the in-plane extensional strains $\varepsilon_{xx}+\varepsilon_{zz}$ corresponds to the two-dimensional divergence. The flow may be considered two-dimensional if $\varepsilon_{xx}+\varepsilon_{zz}=0$ prevails. Finite differencing and standard path integration schemes were used in the estimation of the
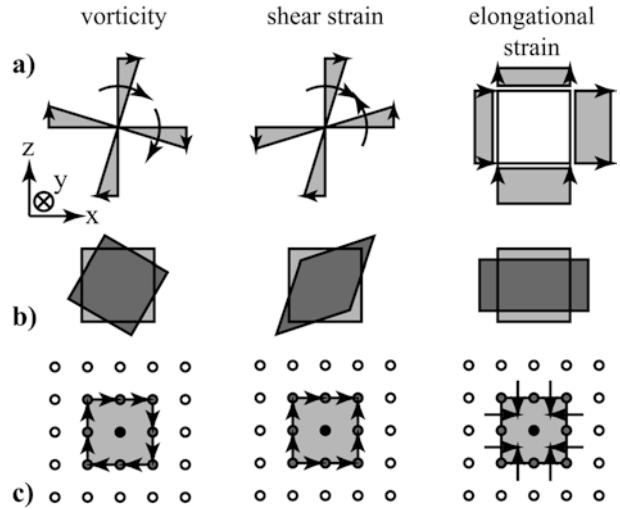

Fig. 7a–c. Differential quantities computed: vorticity, shear strain and elongational strain. a Velocity vector fields resulting in positive differential quantities; b deformation of the fluid element; c implementation of the differential estimators

spatial derivatives of the velocity gradient tensor (Raffel et al. 1998). By definition the vorticity is related to the circulation by the Stokes theorem. The vorticity was determined based on the application of the Stokes theorem with the path integration around a small surface (Landreth and Adrian 1990). The vorticity at a sampling point was estimated by a circulation around the neighboring eight samples as shown in Fig. 7c. The vorticity estimator based on circulation out-performed simple finite difference schemes in a comparison (Westerweel 1993).

4
Wave generation flow fields

4.1
Experimental data
PIV provided instantaneous velocity vector fields in the slide impact area and gave insight into the kinematics of wave generation. A total of 137 experimental runs were conducted and 50 double frames per experiment were acquired at 15 Hz covering a time span of 3.33 s. Each double frame allowed the computation of one velocity vector field. The data comprise experiments with 72 different parameter combinations. In 49 cases, including all investigated parameter combinations at the still-water depths $h=0.30$ m and 0.45 m, juxtaposed areas of view were acquired in repeated experiments. The camera positioning in two subsequent runs with the same experimental parameters is shown in Fig. 8. The adjacent images recorded at the same time in different experiments were mounted together. The enlarged flow fields gave insight into the macro-structure of the flow. Local details along the image joints are corrupted.

Hereafter, only three selected data sequences are presented. Further data analysis was conducted in Fritz (2002b). The slide impact and wave generation flow fields were classified into unseparated and separated flows. At high impact velocities flow separation occurred on the slide shoulder resulting in a hydrodynamic impact crater,
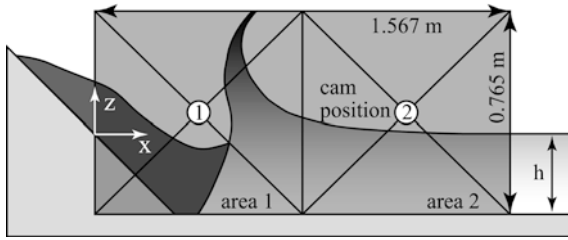
Fig. 8. CCD-camera areas of interest acquired in two repeated runs with the same experimental parameters

whereas at lower impact velocities no flow detachment was observed. Characteristic examples of landslide impacts with and without flow separation as well as a trailing transient bore are presented.

4.2
Unseparated flow

Landslide impacts without flow separation on the slide shoulder were observed at relatively low impact velocities. The unseparated and separated flow regimes were defined primarily based on the slide Froude number **F**. A characteristic example of an unseparated flow around a penetrating landslide at **F**=1.7 is shown in Fig. 9. The set of figures includes the original PIV images, the velocity vector field, streamline plot, and scalar fields of the velocity components. The selected sequence of original PIV recordings is shown in Fig. 9A. The slide thickness increased during the slide penetration (Fig. 9A: *a*). The motion of the slide front created a crest above the slide, while the motion of the back of the slide created a trough (Fig. 9A: *b*). The water displacement was similar to the landslide volume at **F**=1.7. Only a minor addition was due to the trough formed on the back and in the wake of the slide. The detrainment of the air included in the pore volume of the granular slide indicates the presence of a water flow through the slide, since the pore volume had to be filled with water. A massive phase mixing occurred in the wake of the slide (Fig. 9A: *c*). The leading wave crest overtook the slide. Large air bubbles rose out of the back of the slide (Fig. 9A: *d*). The amount of air induced into the water body by the slide detrainment increased proportional to the slide volume in unseparated flows. The air concentration decayed and the second wave was formed by a run-up along the inclined ramp in the wake of the slide and subsequent run-down (Fig. 9A: *c–f*).

The velocity vector fields and the streamline plots revealed the formation of a full saddle point in the back of the slide (Fig. 9B and C: *a,b*). The full saddle propagated outward behind the leading wave crest and down to the channel bottom forming a half saddle (Fig. 9B and C: *c–e*). The half saddle marks the back of the leading wave crest where the water surface crosses the still-water level. Analogously a half saddle formed at the end of the first trough where the water surface crossed the still-water level again (Fig. 9B and C: *f,g*). The half saddles propagated outward along the channel bottom with the wave pattern. The positions of the saddle and half saddles are characterized by instantaneously zero velocity in the scalar fields of the absolute velocities (Fig. 9D). The largest absolute

water particle velocities were measured locally around the slide front during slide penetration. The horizontal particle velocities were zero along vertical lines through the half saddles, whereas the largest values were below the wave crest (Fig. 9E). The water particle velocity was only a fraction of the shallow water wave velocity $(gh)^{1/2}$. It increased with wave height and approached the wave propagation velocity prior to breaking. The vertical particle velocities were zero along vertical lines through the wave crests (Fig. 9F). The largest values were encountered at the location of the largest slope of the water surface.

The computed in-plane divergence was roughly zero in the pure water flow area. Hence the fundamental assumption of the two-dimensional model is confirmed for the pure water flow area. Out-of-plane motion was observed in the massive phase mixing and dissipation area in the wake of the slide. The measurements broke down in the wake of the slide (Fig. 9B: *c–e*). The illumination patterns induced by the rising bubble curtain dominated the PIV image recordings above the slide deposit. Therefore the correlation analysis looked in on the rising bubbles rather than the seeding particles (Fig. 9B: *e–g*). This explains the large vertical velocities above the slide deposit (Fig. 9F: *d–g*).

The computed out-of-plane vorticity in the pure water flow area was roughly zero. This suffices to indicate irrotational flow below the outward propagating impulse waves caused by the zero divergence and hence two-dimensional flow in the pure water flow area. The PIV data confirmed the assumption of irrotation below the water waves, which was made by all analytical wave theories according to the Laplace equation. Significant vorticity was observed on the slide surface because of the shear flow and in the mixing zone above the landslide deposit owing to the dissipative, three-dimensional turbulence.

The computed elongational strains were zero below wave crests and troughs owinf to the horizontal velocity vectors. The elongational strains are largest near the free surface at the locations of the largest gradients in the free surface. The zero contour lines of the shear strain mark the transitions from a wave crest to a trough corresponding roughly to the points where the free surface crosses the imaginary still-water surface. The maximum shear strain values were always encountered below wave crests and troughs.

The wave profile continuously stretched apart over the short sequence and the waves increased in wavelength *L*. The first wave crest and trough have completely different characteristics from the second and following wave crests. The leading wave is an intermediate water depth wave closer to the shallow water wave regime whereas the trailing waves are closer to the deep-water regime. The second wave exhibits the classical wave profile according to Stokes.

4.3
Separated flow

Flow separation on the slide shoulder at high impact velocities resulted in the formation of hydrodynamic impact craters. Backward and outward collapsing impact crater regimes were observed. The slide Froude number
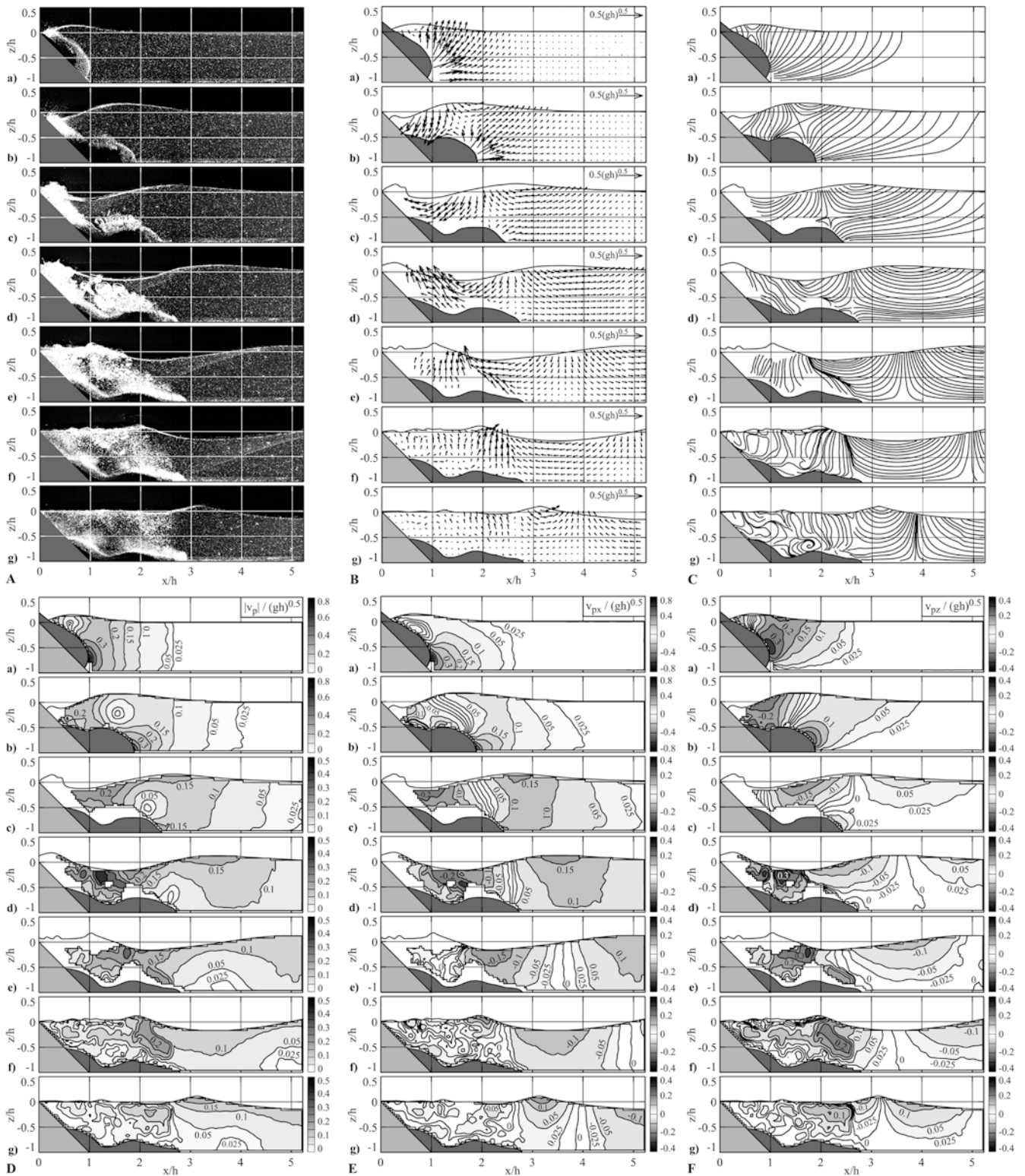
Fig. 9A–F. Unseparated flow. **A** PIV images of two mounted experiments at **F**=1.7, **V**=0.39, **S**=0.19, **h**=0.3 m and $t(g/h)^{0.5}$ *a* 0.93, *b* 2.07, *c* 3.22, *d* 4.36, *e* 5.88, *f* 7.41, *g* 9.7; **B** velocity vector fields; **C** streamlines; **D** absolute particle velocity fields $|v_P|/(gh)^{0.5}$ with contour levels at 0.025, 0.05, 0.1, 0.15, 0.2, 0.3, 0.4, 0.5, 0.6, 0.7, 0.8; **E** horizontal particle velocity fields $v_{px}/(gh)^{0.5}$ with contour levels at 0, ±0.025, ±0.05, ±0.1, ±0.15, ±0.2, ±0.3, ±0.4; **F** vertical particle velocity fields $v_{pz}/(gh)^{0.5}$ with contour levels as in **E**

was the primary classification parameter. A characteristic example of an outward collapsing crater at **F**=4.1 is shown in Fig. 10. The sets of figures include the original PIV images, the velocity vector fields, scalar fields of the

velocity components, and contour plots of the computed components of the deformation tensor. The selected sequences of original PIV recordings are shown in Fig. 10A. The water flow around the penetrating landslide separated
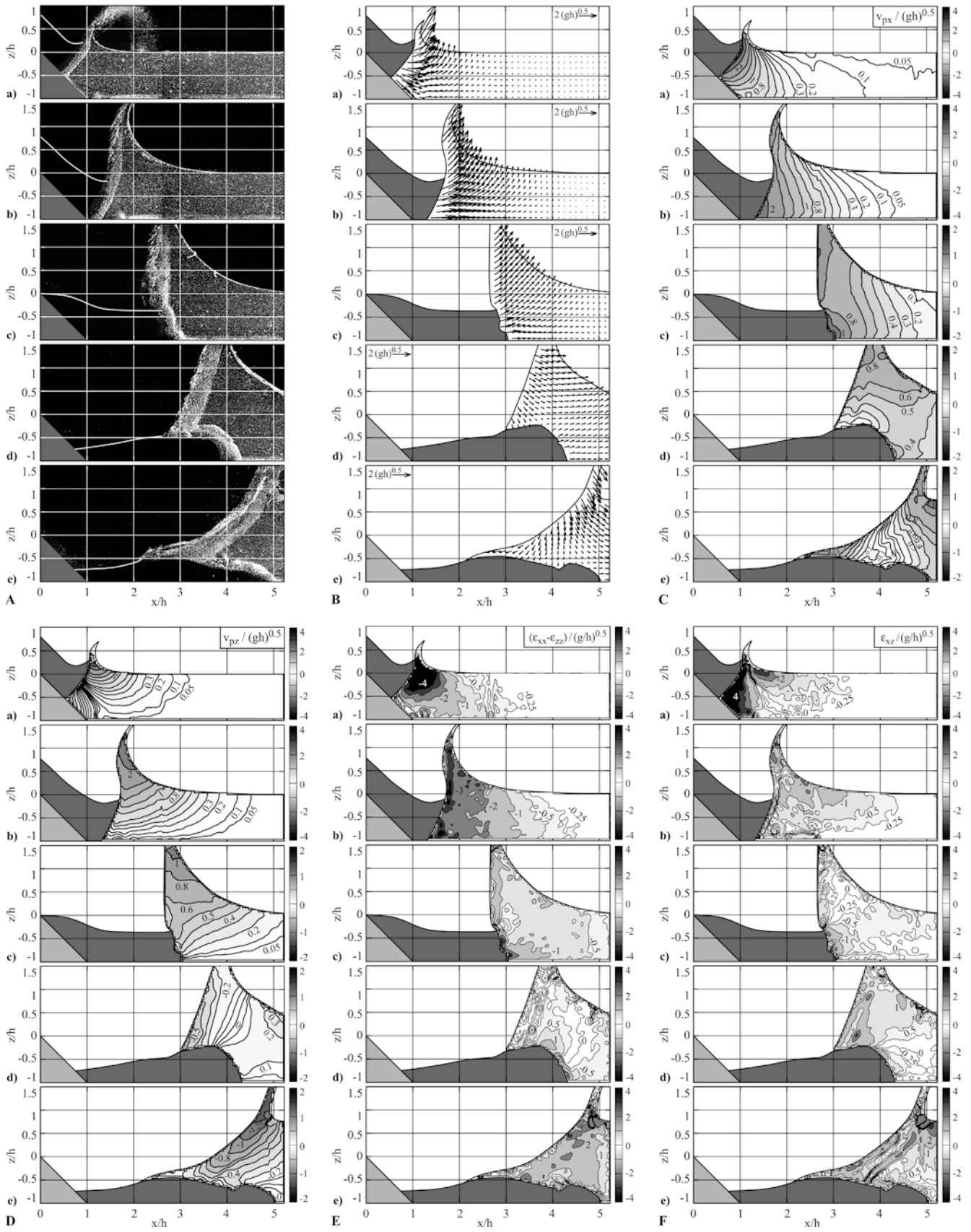
Fig. 10A–F. Outward collapsing impact crater. **A** PIV images of two mounted experiments at **F**=4.1, V=1.57, S=0.56, h=0.3 m and $t(gh)^{0.5}$: a 0.18, b 0.56, c 1.33, d 2.47, e 3.61; **B** velocity vector fields; **C** horizontal particle velocity fields $v_{px}/(gh)^{0.5}$ with contours at 0, ±0.05, ±0.1, ±0.2, ±0.3, ±0.4, ±0.5, ±0.6, ±0.8, ±1, ±1.25, ±1.5, ±2, ±2.5, ±3, ±3.5, ±4; **D** vertical particle velocity fields $v_{pz}/(gh)^{0.5}$ with contour levels as in **C**; **E** elongational strain fields $(\varepsilon_{XX} - \varepsilon_{ZZ})/(g/h)^{0.5}$ with contour levels at 0, ±0.25, ±0.5, ±1, ±2, ±3, ±4; **F** shear strain fields $\varepsilon_{XZ}/\sqrt{g/h}$ with contour levels as in **E**

on the slide shoulder (Fig. 10A: *a–c*). The water was initially expelled upwards and outward by the entry of the landslide forming a water crater. The water crater exposed the ramp and the back of the landslide to the atmosphere. The displaced water volume obviously exceeded the landslide volume significantly. As the process of crater growth has terminated outward, bulk motion of water was still present as a residuum. The crater collapse occurred after the water crater reached its maximum size and the water rushed inward under the influence of gravity. The outward collapsing cavity resulted in a main positive leading wave and negative base surge (Fig. 10A: *d,e*). The inrush of water, which tended to fill the crater from downstream, can qualitatively be viewed as an example of the classical dam break problem (Stoker 1957; Lauber 1997). The backward motion was initiated at the bottom of the crater wall where the hydrostatic pressure was greatest. The leading wave crest was issued by the crater rim and propagated outward during the crater collapse (Fig. 10A: *e*). The run-up of the base surge on the inclined ramp and the subsequent run-down formed the secondary wave system.

The velocity vector fields revealed the formation of a half saddle in the water uplift (Fig. 10B: *d,e*). The half saddle separated the outward from the inward flow. The largest velocities were measured locally around the slide front during slide penetration and in the splash (Fig. 10C and D). The water particle velocity below the wave crest increased compared to the previous examples owing to the increase in wave height. The largest negative values of the horizontal velocity components were observed in the inward rush and run-up along the inclined ramp during the collapse of the impact crater (Fig. 10C: *e*). The negative vertical velocities were observed at the beginning of the crater collapse along the crater walls (Fig. 10D: *e*). Contrary to the classical dam break released from rest, at no instant did the water displaced by the landslide reach a state of sole static uplift. The kinetic energy of the landslide imparted on the water body was only partially converted into the potential energy of the uplift, whereas a significant part prevailed as kinetic energy in the form of the velocity field imposed onto the water body.

The computed in-plane divergence was roughly zero in the pure water flow area confirming the fundamental assumption of the two-dimensional model. Significant divergence values were determined in the phase mixing area because of the air compressibility and the three-dimensional turbulence. The computed out-of-plane vorticity fields indicated that the pure water flow below the outward propagating impulse waves was irrotational. Vorticity was observed on the slide surface caused by the shear flow and in the mixing zone above the landslide deposit owing to the dissipative, three-dimensional turbulence.

The elongational and the shear strain fields are shown in Fig. 10E and F, respectively. The largest negative elongational strains were computed in front of the penetrating landslides were the fluid cells are compressed along the horizontal *x* axis and expanded vertically (Fig. 10E: *a,b*). Large positive elongational strains were measured during the crater collapse caused by the stretching of the fluid

cells along the *x* axis (Fig. 10E: *e*). Large positive shear strain values in the wave field were encountered in the crater rim during collapse and below the wave crests (Fig. 10F: *d,e*). In front of the thick slide positive shear strains were observed (Fig. 10F: *a*), whereas negative values were encountered where the water was uplifted by the slide (Fig. 10F: *a–c*). Both the elongational and the shear strain rates increased compared to the previous examples because of the larger wave heights. Both the elongational and the shear strain rates increased with decreasing wavelength and increasing wave height. Larger strain rates resulted in faster wave attenuations.

4.4
Secondary bore formation

A bore formed as the second outward propagating wave after the impact crater had collapsed and the first wave had propagated out of the impact area. A characteristic example of a transient bore is shown in Fig. 11. The sets of figures include the original PIV images, the velocity vector fields, the streamline plots, scalar fields of the velocity components, and vorticity contour plots. The selected sequences of original PIV recordings are shown in Fig. 11A. The landslide impact at **F**=4.7 shown previously to the image sequence caused an outward collapsing impact crater analogous to the preceding example shown in Fig. 10. The presented sequence begins with the first wave trough after the leading wave crest had left the area of view to the right, and the backward run-up along the inclined ramp had reached its highest point (Fig. 11A: *a*). The local reduction in water level following the first wave crest caused by the inrush of water is transmitted outwards as a wave trough. The inward motion along the channel bottom collides with the run-down forming a surge (Fig. 11A: *b,c*). The surge propagating outward on top of the backward flow is analogous to a transient bore (Fig. 11A: *d–g*). A key feature is the dissipation process during its early phase. While the collapse of the crater itself is not dissipative, a considerable portion of the energy imparted to the fluid is lost as a result of turbulent mixing at the impact site from the rebound of the inward flow. The energy dissipated by the turbulent mixing was not determined experimentally because the measurement area was too small to extract both the potential and kinetic energy of the whole impact crater rim.

The energy dissipation in a transient bore was computed numerically with the momentum and Bernoulli's theorem by LeMéhauté and Khangoankar (1992). In contrast with the trivial solutions of a hydraulic jump the full form of the equations including the unsteady terms had to be solved numerically. The energy that dissipated hydrodynamically remained constant at roughly 40% of the potential and kinetic energies initially transmitted to the fluid by the landslide, independent of the lip shape (Fritz 2002b). The bore propagated outward roughly at $\sqrt{gh}$. As the bore propagates and decays, it is transformed into a non-breaking (non-dissipative) bore and finally a nonlinear wave. When the underlying incoming flow reaches subcritical conditions, or the bore height becomes smaller than 60% of the incoming flow depth, the dissipative bore no longer exists (Favre 1935). It is then transformed into a
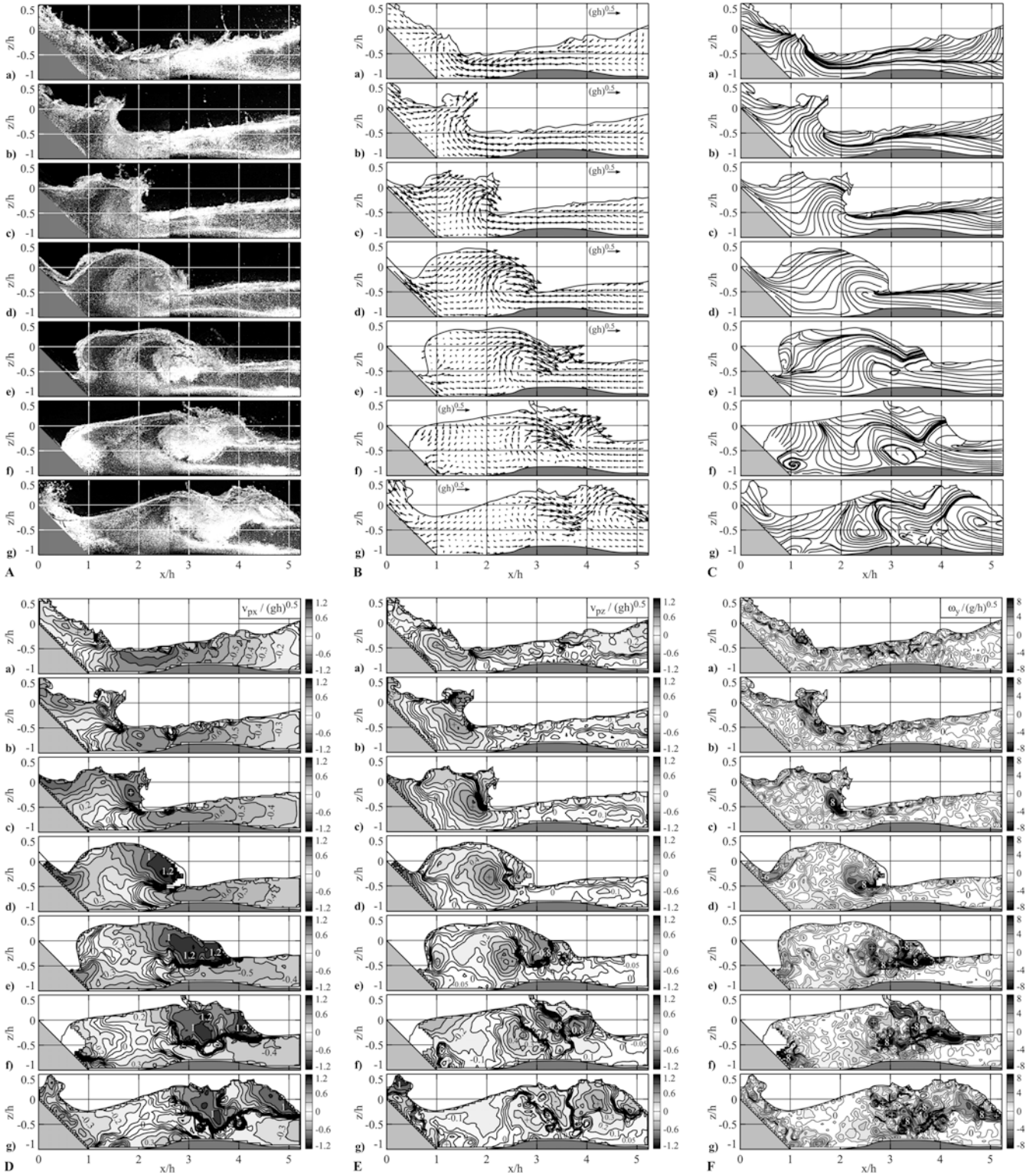
Fig. 11A–F. Secondary bore formation. **A** PIV images of two mounted experiments at F=4.7, V=0.39, S=0.17, h=0.3 m and t(g/h)^0.5: a 6.97, b 7.73, c 8.49, d 9.25, e 10.01, f 10.78, g 11.51; **B** velocity vector fields; **C** streamlines; **D** horizontal particle velocity fields $v_{px}/(gh)^{0.5}$: contours at 0, ±0.05, ±0.1, ±0.2, ±0.3, ±0.4, ±0.5, ±0.6, ±0.8, ±1, ±1.2; **E** vertical particle velocity fields $v_{pz}/(gh)^{0.5}$ with contour levels as in **D**; **F** vorticity fields $\omega_y/(g/h)^{0.5}$ with contour levels at 0, ±0.5, ±1, ±2, ±3, ±4, ±6, ±8

translatory non-dissipative undulating bore, which follows the leading wave at a distance.

The velocity vector fields and the streamline plots reveal the internal flow structure during the formation and propagation of a transient bore (Fig. 11B and C). The half saddle along the ramp marked the collision between the run-down and the inward rush resulting in a spike at the free surface (Fig. 11B and C: a,b). The half saddle propagated outward with the bore (Fig. 11B and C: c–g). The largest velocities were measured locally along the ramp

and in the breaking bore (Fig. 11D and E). The horizontal water particle velocity in the bore exceeded even the shallow water wave velocity $\sqrt{gh}$ computed with the still-water depth (Fig. 11D: *d–f*). The vertical velocity in the bore was smaller than the horizontal component (Fig. 11E).

The in-plane divergence field was significantly noisier than for the previous examples because of the massive phase mixing and the air entrainment during the bore formation. The computed out-of-plane vorticity fields are shown in Fig. 11F. In contrast with the previous mainly irrotational waves the bore formation involved large positive vorticity values similar to the wave breaking process (Fig. 11F: *c–g*). The assumption of irrotational flow does not hold for bores. Further the bore was characterized by positive elongational strains on top of a layer with negative values near the bottom. The negative elongational strains marked water cells being compressed along the *x* axis and expanded upward because of the collision between the inward flow and the run-down. The shear strain was positive under the bore as under a wave crest.

5
Conclusions

The initial phase of landslide generated impulse waves in reservoirs, lakes, bays, or oceans was investigated in a two-dimensional physical laboratory model based on the generalized Froude similarity. Landslides were successfully modeled with an artificial granular material consisting of barium-sulfate and polypropylene (PP-BaSO$_4$). The developed pneumatic landslide generator was able to control the slide impact characteristics, thus allowing exact reproduction and independent variation of single dynamic slide parameters. The results of the experimental study regarding the instantaneous flow fields of the slide impact and wave generation may be summarized as follows:

— PIV was successfully applied to individual areas of view up to 0.8 m×0.8 m in the impact and wave generation zones characterized by large velocity gradients near the interface between the water and the slide, as well as massive mixing of the three phases: water, slide granulate, and entrained air.
— Digital masking techniques were applied to distinguish between phases thus allowing phase separated image processing. PIV is ideally suited to the analysis of instantaneous flow fields in extremely unsteady flows.
— The performance of the large-scale PIV system was determined with regard to the DVR, spatial resolution and measurement accuracy.
— The macro-structure of the flow in the impact and wave generation area was determined with PIV. Mounted areas of view resulted in 49 flow map sequences covering 1.6 m×0.8 m. The following flow maps were computed: velocity vector, streamline, absolute velocity, horizontal and vertical particle velocity, in-plane divergence, out-of-plane rotation, and elongational and shear strain rate.
— Examples of an unseparated flow, a separated flow with an outward collapsing hydrodynamic impact crater,

and the formation of a dissipative transient bore as a secondary wave were presented.
— The water displacement significantly exceeded the landslide volume in cases with flow separation and impact crater formation.
— The in-plane divergence was roughly zero in the pure water flow area confirming the two-dimensional model assumption. Out-of-plane motion was observed in the wake of the slide and the massive phase mixing area.
— The out-of-plane vorticity was roughly zero in the pure water flow area below the outward propagating water waves. The non-breaking landslide generated impulse waves are irrotational. The assumption of irrotationality does not hold for breaking waves and bores, which involve large positive vorticity. Significant vorticity was observed in the shear flow on the slide surface and the massive phase mixing area.
— Elongational and shear strains governed the flow fields in both the impulse wave generation and propagation zones. The elongational strains are zero below wave crests and troughs because of the horizontal velocity vectors and largest near the free surface at the locations of the largest gradients in the free surface. The maximum shear strain values are always encountered below wave crests and troughs. Both the elongational and the shear strain rates increased with decreasing wavelength and increasing wave height.

References

Adrian RJ, Yao C-S (1985) Pulsed laser technique application to liquid and gaseous flows and the scattering power of seed materials. Appl Optics 24:44–52

Adrian RJ (1991) Particle-imaging techniques for experimental fluid mechanics. Ann Rev Fluid Mech 23:261–304

Adrian RJ (1995) Limiting resolution of particle image velocimetry for turbulent flow. In: Proceedings of the 2nd Turbulence Research Association Conference—I. Pohang Institute of Technology, Pohang, Korea, 1–19

Adrian RJ (1997) Dynamic ranges of velocity and spatial resolution of particle image velocimetry. Meas Sci Technol 8:1393–1398

Bohren CF, Huffman DR (1998) Absorption and scattering of light by small particles, 3rd edn. Wiley, New York

De Quervain F (1980) Tabellen zum Mineral- und Gesteinsbestimmen, 3rd edn. Verlag der Fachvereine VdI, Zürich

Favre H (1935) Étude théorique et expérimentale des ondes de translation dans les canaux découverts. Dunod, Paris

Fincham AM, Delerce G (2000) Advanced optimization of correlation imaging velocimetry algorithms. Exp. Fluids 29:S13–S22

Fritz HM, Hager WH, Minor H-E (2001) Lituya Bay case: rockslide impact and wave run-up. Sci Tsunami Haz 19:3–22

Fritz HM (2002a) PIV applied to landslide generated impulse waves. In: Adrian RJ et al. (eds) Laser techniques for fluid mechanics. Springer, New York Berlin Heidelberg, 305–320

Fritz HM (2002b) Initial phase of landslide generated impulse waves. Dissertation, ETH No 14'871, Swiss Federal Institute of Technolgy, Zürich

Fritz HM, Moser P (2003) Pneumatic landslide generator. Int J Fluid Power 4:49–57

Glicken H (1996) Rockslide-debris avalanche of May 18, 1980, Mount St. Helens Volcano, Washington. U.S. Geological Survey Open-File Report 96–677

Goodman JW (1996) An introduction to Fourier optics. McGraw-Hill, New York

Gray C, Greated CA (1988) The application of particle image velocimetry to the study of water waves. Optics Lasers Eng 9:265–276

Gray C, Greated CA, McCluskey DR, Easson WJ (1991) An analysis of the scanning beam PIV illumination system. Meas Sci Technol 2:717–724

Hart DP (1998) Super-resolution PIV by recursive local correlation. In: Proceedings of the International Conference on Optical technology and image processing in fluid, thermal and combustion flow, Yokohama, Japan, 6–10 December 1998.VSJ–SPIE98, AB149:1–10

Hecht E (1998) Optics, 3rd edn. Addison-Wesley, Reading, Mass

Hecht J (1992) The laser guidebook, 2nd edn. McGraw-Hill, New York

Hering F, Leue C, Wierzimok D, Jähne B (1997) Particle tracking velocimetry beneath water waves. Part 1: visualization and tracking algorithms. Exp Fluids 23:472–482

Hinze JO (1975) Turbulence, 2nd edn. McGraw-Hill, New York

Hjelmfelt AT, Jr, Mockros LF (1966) Motion of discrete particles in a turbulent fluid. Appl Sci Res 16:149–161

Holst GC (1998) CCD arrays, cameras and displays. SPIE Optical Engineering Press, Bellingham, Wa

Huang HT, Fielder HF, Wang JJ (1993a) Limitation and improvement of PIV. Part I: limitation of conventional techniques due to deformation of particle image patterns. Exp Fluids 15:168–174

Huang HT, Fielder HF, Wang JJ (1993b) Limitation and improvement of PIV. Part II: particle image distortion, a novel technique. Exp Fluids 15:263–273

Huang HT, Dabiri D, Gharib M (1997) On errors of digital particle image velocimetry. Meas Sci Technol 8:1427–1440

Huber A (1980) Schwallwellen in Seen als Folge von Bergstürzen. In: Vischer D (ed) VAW-Mitteilung 47. Versuchsanstalt für Wasserbau, Hydrologie und Glaziologie, ETH Zürich

Jähne B (1997) Digital image processing—concepts, algorithms, and scientific applications, 4th edn. Springer-Verlag, Berlin Heidelberg New York

Jensen A, Sveen JK, Grue J, Richon J-B, Gray C (2001) Accelerations in water waves by extended particle image velocimetry. Exp Fluids 30:500–510

Keane RD, Adrian RJ (1990) Optimization of particle image velocimeters. Part 1: Double pulsed systems. Meas Sci Technol 1:1202–1215

Keane RD, Adrian RJ (1992) Theory of cross-correlation analysis of PIV images. Appl Sci Res 49:191–215

Kerker M (1969) The scattering of light. Academic Press, New York

Kündig R, Mumenthaler T, Eckardt P, Keusen HR, Schindler C, Hofmann F, Vogler R, Guntli P (1997) Die mineralischen Rohstoffe der Schweiz. Schweizerische Geotechnische Kommission, Zürich

Landreth CC, Adrian RJ (1990) Impingement of a low Reynolds number turbulent circular jet onto a flat plate at normal incidence. Exp. Fluids 9:74–84

Lauber G (1997) Experimente zur Talsperrenbruchwelle im glatten geneigten Rechteckkanal. In: Vischer D (ed) VAW-Mitteilung 152. Versuchsanstalt für Wasserbau, Hydrologie und Glaziologie, ETH Zürich

LeMéhauté B, Khangoankar T (1992) Generation and propagation of explosion generated waves in shallow water. Technical Report DNA-TR-92-40, Nuclear Defense Agency, Washington D.C

Lin P, Chang K-A, Liu PL-F (1999) Runup and rundown of solitary waves on sloping beaches. J Waterway Port Coastal Ocean Eng ASCE 125:247–255

Lindken R, Merzkirch W (2000) Velocity measurements of liquid and gaseous phase for a system of bubbles rising in water. Exp Fluids 29:S194-S201

Liu A, Shen X, Smith GH, Grant I (1992) Particle image velocimetry measurements of wave–current interaction in a laboratory flume. Optics Lasers Eng 16:239–264

Melling A (1997) Tracer particles and seeding for particle image velocimetry. Meas Sci Technol 8:1406–1416

Mie G (1908) Beiträge zur Optik trüber Medien, speziell kolloidaler Metallösungen. Ann Phys 25:377–445

Müller D (1995) Auflaufen und Überschwappen von Impulswellen an Talsperren. In: Vischer D (ed) VAW-Mitteilung 137. Versuchsanstalt für Wasserbau, Hydrologie und Glaziologie, ETH Zürich

Nogueira J, Lecuona A, Rodríguez PA (1997) Data validation, false vectors correction and derived magnitudes calculation on PIV data. Meas Sci Technol 8:1493–1501

Prasad AK, Adrian RJ, Landreth CC, Offutt PW (1992) Effect of resolution on the speed and accuracy of particle image velocimetry interrogation. Exp Fluids 13:105–116

Raffel M, Willert CE, Kompenhans J (1998) Particle image velocimetry—a practical guide. Springer, Berlin Heidelberg New York

Roth GI, Mascenik DT, Katz J (1999) Measurements of the flow structure and turbulence within a ship bow wave. Phys Fluids 11:3512–3523

Scarano F, Riethmuller ML (1999) Iterative multigrid approach in PIV image processing with discrete window offset. Exp Fluids 26:513–523

Scarano F, Riethmuller ML (2000) Advances in iterative multigrid PIV image processing. Exp Fluids 29:S51–S60

Savage SB (1979) Gravity flow of cohesionless granular materials in chutes and channels. J Fluid Mech 92:53–96

Shifrin KS (1988) Physical optics of ocean water. AIP translation series. American Institute of Physics, New York

Skyner D (1996) A comparison of numerical predictions and experimental measurements of the internal kinematics of a deep-water plunging wave. J Fluid Mech 315:51–64

Slingerland RL, Voight B (1979) Occurrences, properties and predictive models of landslide-generated impulse waves. Rockslides and avalanches—2. In: Voight B (ed) Developments in geotechnical engineering, vol 14B. Elsevier, Amsterdam, 317-397

Son SY, Kihm KD (2001) Evaluation of transient turbulent flow fields using digital cinematographic particle image velocimetry. Exp. Fluids 30:537–550

Stoker JJ (1957) Water waves. Interscience, New York

Tognacca C (1999) Beitrag zur Untersuchung der Entstehungsmechanismen von Murgängen. In: Minor H-E (ed) VAW-Mitteilung 164. Versuchsanstalt für Wasserbau, Hydrologie und Glaziologie, ETH Zürich

van de Hulst HC (1957) Light scattering by small particles. Wiley, New York

Varnes DJ (1978) Slope movements types and processes. In: Shuster RL, Krizek RJ (eds) Landslides analysis and control. Transportation Research Board Special Report 176:11–33

Vischer DL, Hager WH (1998) Dam hydraulics. Wiley, Chichester

Wernet M, Pline A (1993) Particle displacement tracking technique and Cramer–Rao lower bound error in centroid estimates from CCD imagery. Exp Fluids 15:295–307

Westerweel J (1993) Digital particle image velocimetry: theory and application. Delft University Press, Delft

Westerweel J (1994) Efficient detection of spurious vectors in particle image velocimetry data. Exp Fluids 16:236–247

Westerweel J, Dabiri D, Gharib M (1997) The effect of a discrete window offset on the accuracy of cross-correlation analysis of digital PIV recordings. Exp Fluids 231:20–28

Westerweel J (2000) Theoretical analysis of the measurement precision in particle image velocimetry. Exp Fluids 29:S3–S12

Willert CE, Gharib M (1991) Digital particle image velocimetry. Exp Fluids 10:181–193